



# Optimal structural characteristics of osteoinductivity in bioceramics derived from a novel high-throughput screening plus machine learning approach

Yunyi Liu <sup>b,c</sup> , Quanle Cao <sup>b,c</sup>, Shengyi Yong <sup>b,c</sup>, Jing Wang <sup>b,c</sup>, Xuening Chen <sup>a,b,c</sup>, Yumei Xiao <sup>a,b,c</sup>, Jiangli Lin <sup>a,c</sup>, Mingli Yang <sup>a,c</sup> , Kefeng Wang <sup>a,b,c,\*</sup>, Xiangfeng Li <sup>a,b,c,\*\*</sup> , Xiangdong Zhu <sup>a,b,c,\*\*\*</sup> , Xingdong Zhang <sup>a,b,c</sup>

<sup>a</sup> Provincial Engineering Research Center for Biomaterials Genome of Sichuan & Research Center for Material Genome Engineering, Sichuan University, Chengdu, 610064, China

<sup>b</sup> National Engineering Research Center for Biomaterials, Sichuan University, Chengdu, 610064, China

<sup>c</sup> College of Biomedical Engineering, Sichuan University, Chengdu, 610064, China

## ARTICLE INFO

### Keywords:

Osteoinductivity  
Calcium phosphate ceramics  
3D printing  
High throughput screening  
Correlation analysis

## ABSTRACT

Osteoinduction is an important feature of the next generation of bone repair materials. But the key structural factors and parameters of osteoinductive scaffolds are not yet clarified. This study leverages the efficiency of high-throughput screening in identifying key structural factors, performs screening of 24 different porous structures using 3D printed calcium phosphate (CaP) ceramic scaffolds. Based on *in vitro* and *in vivo* evaluations, along with machine learning and nonlinear fitting, it explores the complex relationship between osteoinductive properties and scaffold configurations. Results indicate that bone regenerative ability is largely affected by porosity and specific surface area (SSA), while pore geometry has a negligible effect. The optimal structural parameters were identified as a porous structure with SSA of 10.49–10.69 mm<sup>2</sup> mm<sup>-3</sup> and permeability of 3.74 × 10<sup>-9</sup> m<sup>2</sup>, which enhances osteoinductivity and scaffold properties, corresponding to approximately 65%–70% porosity. Moreover, nonlinear fitting reveals specific correlations among SSA, permeability and osteogenic gene expressions. We established a data-driven high-throughput screening methodology and proposed a parametric benchmark for osteoinductive structures, providing critical insights for the design of future osteoinductive scaffolds.

## 1. Introduction

Bones possess remarkable self-healing capabilities. However, defects beyond a critical size can impede this process and lead to non-union [1]. Over recent decades, numerous scaffolds have been developed as substitutes to aid in the repair and regeneration of bone tissue [2]. Among these, porous scaffolds are notable for their superior biocompatibility and three-dimensional structures, which mimic extracellular microenvironment to support cellular activities and new tissue growth [3]. The interconnected pores within these scaffolds enhance the transport of nutrients and oxygen, facilitating cellular migration and tissue

formation. Research has highlighted that the size, shape, and structure of the pores are critical in optimizing new bone formation, vascularization, and bone remodeling [4–6]. In the field of bone repair scaffolds, calcium phosphate (CaP) bioceramics have been highly favored by researchers over the past decade due to their excellent bioactivity and biodegradability. They have been safely used to fill various bone defects. Additionally, studies revealed that CaP ceramics possessed osteoinductive properties that promote osteogenesis and osseointegration. It's well accepted that porous structure has a critical impact on osteoinductivity. For instance, Shi's study found that hydroxyapatite porous scaffolds with large pore sizes (1200–1500 μm) had more new bone formation

\* Corresponding author. National Engineering Research Center for Biomaterials, Sichuan University, Chengdu, 610064, China.

\*\* Corresponding author. College of Biomedical Engineering, Sichuan University, Chengdu, 610064, China.

\*\*\* Corresponding author. Provincial Engineering Research Center for Biomaterials Genome of Sichuan & Research Center for Material Genome Engineering, Sichuan University, Chengdu, 610064, China.

E-mail addresses: [fencal@scu.edu.cn](mailto:fencal@scu.edu.cn) (K. Wang), [hkdlxiangfeng@163.com](mailto:hkdlxiangfeng@163.com) (X. Li), [zhu\\_xd1973@scu.edu.cn](mailto:zhu_xd1973@scu.edu.cn) (X. Zhu).

and more uniform new bone distribution than other scaffolds [7]. Wu's study evaluated the osteoinduction ability of four biphasic calcium phosphate (BCP) ceramic scaffolds with varying pore geometries, showing that the hexagonal close-packed (HCP) spherical pore structure exhibited outstanding osteoinductivity [8]. However, the complexity and diversity of pore structure led to vague relationship between pore structure and osteoinductivity. There is still a lack of guidelines and data support for the structural design of scaffolds, which hinders the advancement of high-performance bone regeneration.

In the last five years, 3D printing, particularly Digital Light Processing (DLP), offers high resolution and rapid prototyping for the creation of bioceramic scaffolds [9]. In our previous work, various pore-structured CaP ceramics were prepared using DLP 3D printing [10]. Importantly, it makes efficient screening of bioceramic structures possible. Nowadays, high-throughput screening offers a transformative approach by enabling the rapid evaluation of a large number of scaffold designs in parallel, greatly improving the efficiency of parameter screening and structure-activity relationship (SAR) analysis. Initially, researchers used these methods for synthesizing small molecules, such as enzymes and peptides [11]. Then they evolved rapidly and were extensively used in discovering and developing novel biomaterials for applications in cell therapy, tissue engineering, gene therapy and regenerative medicine [12]. For example, van der Boon [13] utilized polydimethylsiloxane substrates with specific gradient wrinkle morphologies in conjunction with a bottomless 96-well plate to explore the effects of micro and nano-surface morphologies on human BMSC cells. High-throughput screening is also applied to the evaluation of *in vivo* experiments. Oliveira [14] developed the technique by implanting microarray chips containing 36 different scaffolds in Wistar rats. It can detect hit points with good characteristics and significantly reduce the use of laboratory animals. High-throughput techniques significantly enhance experimental efficiency and reduce costs, enabling researchers to quickly gather a wealth of data and gain a deeper understanding of the properties and mechanisms of materials [12]. It can drive innovation, provide guidance and establish structure-activity and dose-response relationships between different characteristics, in which analyzing various data features is crucial, particularly the nonlinear interactions. Machine learning (ML) excels at uncovering and predicting

the intricate structure-activity relationships between material properties and characterization outcomes, without requiring prior knowledge [15, 16]. Biomaterial features are associated as input data with cell behavior and *in vivo* experimental results, and computational simulations based on ML algorithms and mathematical modeling are used to process these data [17]. Horikawa [18] constructed a ML model to predict the osteogenic ability of bioceramics, and predicted the properties and osteogenic rate of the materials through the inverse analysis of the constructed mode. The AI-assisted High-throughput 3D Printing Condition Screening System (AI-HTPCSS) integrates a programmable pneumatic extrusion printer with AI-driven image analysis, enabling up to 45120 printing conditions to be screened daily. Scaffold produced under optimized conditions demonstrated robust mechanical properties and accelerated diabetic wound healing *in vivo* [19]. In our previous work, various ML models have been employed to predict the osteoinductive performance of biomaterials [20]. Based on experimental results and literature review, it has been found that in scenarios involving complex interactions among multiple variables, such as predicting blood pressure during hemodialysis [21] or diagnosing chronic kidney disease [22], the XGBoost model offers higher prediction accuracy and overcomes the limitations of simple linear models. This capability provides invaluable assistance in interpreting high-throughput experimental data and material property optimization.

In this study, based on the high-throughput method and DLP 3D printing technology, the structural parameters of CaP ceramic scaffolds were screened to identify and establish their structure-activity relationship with osteoinduction (Fig. 1). CaP Chip/Cyl-scaffold integrated with 24 distinct pore structures were fabricated. The impact of pore configurations on osteoinductivity was evaluated through co-culture with BMSCs and intramuscular implantation *in vivo*. ML was adopted to fit the nonlinear relationship between material characteristics and osteogenic activity, and the influence of material structural factors on osteoinductivity was further discussed. It's expected to obtain and identify optimal structural parameters for osteoinductive biomaterials, providing a swift and efficient method to generate substantial data and design guidance for osteoinductive scaffolds, which will expedite the advancement of bone regenerative biomaterials.

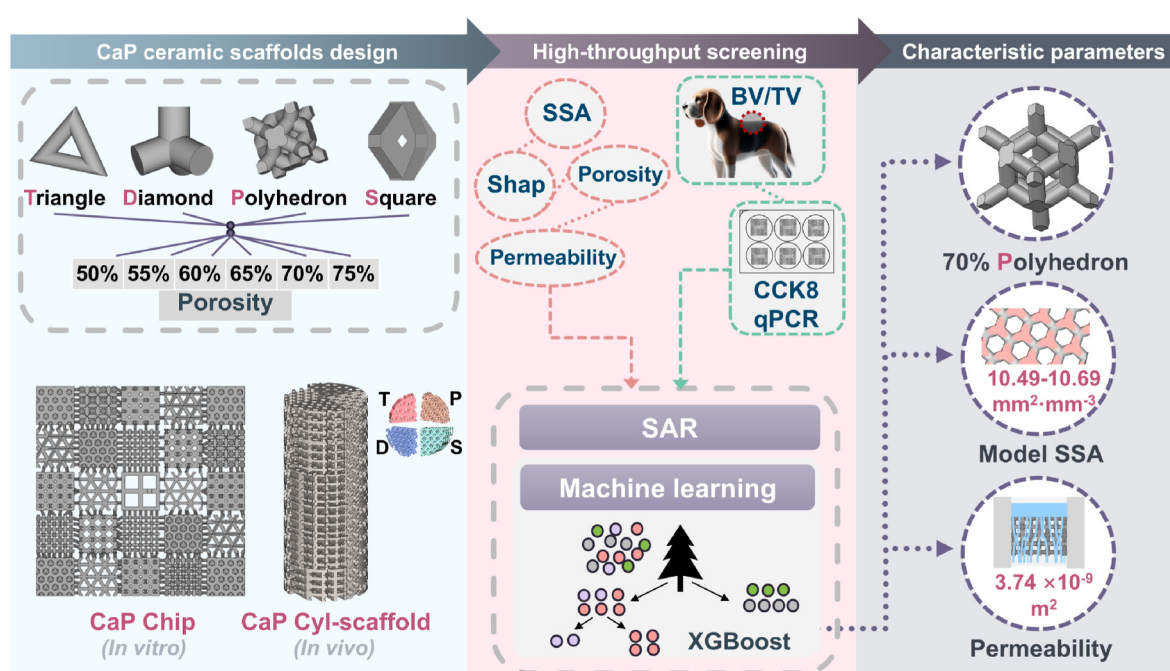


**Fig. 1.** Schematic diagram of the design of DLP-based 3D printed CaP Chip/Cyl-scaffold.

## 2. Methods

### 2.1. Design of high-throughput screening

Two types of integrated ceramic scaffolds (chip scaffold (CaP Chip) and cylindrical scaffold (CaP Cyl-scaffold)), each consisting of 24 structures designed for *in vitro* and *in vivo* experiments. The scaffolds included triangular (T), diamond (D), square (S), and polyhedral (P) structures, each featuring six porosity levels ranging from 50 % to 75 %, as shown in Fig. 1. The *in vitro* experimental scaffold, called CaP Chip, is integrated in a planar manner. The 24 structures are arranged according to the order shown in the figure, forming a 5 × 5 chip plane. Leveraging the advantages of DLP-based 3D printing technology, the structures are connected by small connecting rods (500 µm). All these rods were connected using the nearest connection method. Firstly, the suspended end points caused by structure cutting are integrated and repaired, and then the end points of adjacent structures are connected in two directions to ensure that all the end points between the structures are connected. For *in vitro* cell culture, single-well culture can be achieved to eliminate the influence of different environments and surface microstructures on cell experiment results, focusing solely on the effect of the structure on BMSCs. The connecting rods facilitate efficient characterization in different experiments. For example, in live/dead assays, the complete structure can be stained and photographed. In CCK8 and qRT-PCR experiments, the structures can be easily separated with a sterile blade for individual experiments and characterization. This design not only enables high-throughput and efficient experiments but also adapts to different testing instruments. For *in vivo* experiments, the CaP Cyl-scaffold design features a closely packed 4 × 6 arrangement to form a cylindrical scaffold, which is more suitable for animal implantation experiments. After the entire CaP Cyl-scaffold was scanned via micro-CT, it was easily cut and sectioned for subsequent staining.

### 2.2. CaP ceramics 3D printing of CaP ceramics

CaP ceramics were fabricated using DLP-based 3D printing technology. The raw CaP powders were provided by the National Engineering Research Center for Biomaterials, Sichuan University. The printing slurry consisted of monoalcohol ethoxylate phosphate (MAEP)-modified CaP powders (42 wt %), photosensitive resin, and toners. The CaP Chip and Cyl-scaffold were designed using 3D modeling software (SolidWorks, Dassault Systèmes, France). The designed model structure file was saved in STL format, imported into model processing software (10 Dim, TEN DIMENSIONS, China) suitable for the Autocera-M printer, and then sliced into ultrathin layers with a thickness of 50 µm. The 3D printing process was carried out to prepare the ceramic green bodies. After printing, the CaP ceramic green bodies were immersed in absolute ethanol for 15 min with ultrasound to thoroughly clean the unsolidified slurry, followed by secondary curing. Subsequently, the ceramic green bodies were placed in a muffle furnace and sintered at 1150 °C for 2 h. The size of CaP Chip for *in vitro* experiments were set to 23.5 mm × 23.5 mm × 4 mm (4.3 mm × 4.3 mm × 4 mm/Unit), while for *in vivo* animal experiments, the CaP Cyl-scaffold size was set to 10 mm × 24 mm (Ø × h) (4 mm/Layer).

### 2.3. Characterization of 3D-printed CaP ceramics

The microscopic morphology of CaP ceramics was visualized by using a field emission scanning electron microscope (FE-SEM, JSE-5900LV, Japan). The phase compositions of CaP ceramic were analyzed with X-ray diffraction (XRD, Shimadzu XRD6100, Japan). The specific surface area (SSA) and porosity of these 24 different porous ceramic bodies were calculated by the designed model structure file. The falling head method [23] was employed to assess the permeability of the structures. Each ceramic body was placed in a customized apparatus, and red ink was introduced from above. And three parallel samples of

these 24 different porous ceramic bodies were tested to ensure the validity of the results. Subsequently, the difference in liquid level and the time taken for it to descend were recorded. These measurements were used to calculate the permeability of these 24 different porous ceramic bodies.

### 2.4. Cell proliferation and morphology

Cell proliferation was analyzed using a cell counting kit-8 (Beyotime Biotechnology, China) assay on days 3, 7, and 14. Absorbance was measured at a wavelength of 450 nm with a microplate reader (Varioskan Flash, Thermo Scientific, USA). After culturing for 3, 7, 14 and 21 days, living and dead cells were stained with fluorescein diacetate and propidium iodide (FDA/PI, Topbio Science, China). The living cells (green) and dead cells (red) were then observed and photographed using a laser confocal microscope (Zeiss, SM 800, Germany).

### 2.5. Quantitative real-time reverse-transcription PCR (qRT-PCR) verification

To investigate whether different bioceramic granules could enhance the osteogenic of the cells, the CaP Chip was cocultured with BMSCs. The gene expressions of key osteogenic genes, including alkaline phosphatase (ALP), osteocalcin (OCN), runt-related transcription factor 2 (Runx-2), collagen type I (COL-I) and osteopontin (OPN) in BMSCs was analyzed, primers listed in Table S1. Briefly, total RNA was extracted using the RNAiso Plus reagent (Tiangen Biomedical Technology, China). The extracted RNA samples were reverse transcribed into complementary DNA (cDNA) with the iScript™ cDNA Synthesis kit (Bio-Rad, USA), and this reaction was performed using the CFX96t real-time PCR detection system (CFX960, Bio-Rad, USA) with SsoFast™ EvaGreen® Supermix (Bio-Rad, USA). The amplification procedure was performed under the following conditions: 95 °C for 2 min incubation, followed by 40 cycles of 95 °C for 2 s and 60 °C for 5 s. The relative fold changes were calculated using the comparative quantity  $\Delta\Delta Ct$  method. GAPDH was chosen as the housekeeping gene to normalize the expression levels of the target genes.

### 2.6. Surgical procedures

The animal experiment protocol received approval from the Institutional Animal Care and Use Committee (IACUC) of Sichuan University (SCXK2020-232). The study involved implanting CaP Cyl-scaffold devices into the dorsal muscles of beagles (body weight: 10 kg; gender: male) for a duration of 180 days to evaluate osteoinduction. This timeframe is consistent with established practices and allows for an adequate assessment of the osteoinductive capabilities of the CaP Cyl-scaffold as well as their biocompatibility. The procedure was conducted under anesthesia using 0.3 % pentobarbital sodium administered at a dose of 10 mg/kg body weight into the great saphenous vein of the hind limb. A 10 mm longitudinal skin incision was made along the spinal line using a scalpel, and the samples ( $n = 3$ ) were subsequently implanted into the muscle. After 180 days post-surgery, the beagles were humanely euthanized, and the implants were extracted and immersed in 4 % paraformaldehyde for preservation and further analysis.

### 2.7. Micro-computed tomography (micro-CT) analysis

High-resolution micro-computed tomography imaging ( $\mu$ CT80, Scanco Medical, Basersdorf, Switzerland) was employed to assess new bone formation within the porous materials. The X-ray tube was set to 70 kV and 114 µA, with an integration time of 300 ms per sample. The scan region had a resolution of 2048 × 2048 pixels, producing greyscale images with a resolution of 15 µm. These images were reconstructed and analyzed using Scanco software. Thresholding was applied to differentiate the signals from the ceramic scaffold and the newly formed bone.

Additionally, three parameters were quantified: the volumes of newly formed bone (BV) in the different structures and the total volume of tissues (TV) in each structure. The new bone substitution rate was calculated as the ratio BV/TV. This ratio was used to describe the changes in each region within the multi-structure before and after implantation.

### 2.8. Histological analysis

After micro-CT analysis, the samples were dehydrated in ascending concentrations of alcohol (70 %–100 %) three times. The samples were then embedded in resin. Transverse sections (7  $\mu\text{m}$  thick) were cut from the embedded tissues using a motorized microtome. Hematoxylin and eosin (H&E) staining was performed on sections from each sample, and the stained sections were observed with a pathological section scanner Pannoramic MIDI (VS200, Olympus, Japan).

### 2.9. Pearson correlation coefficient

The Pearson correlation coefficient was employed to measure that quantifies the strength and direction of the linear relationship between the input variables and output variables. The correlation coefficient value, was calculated according to Eq. (1):

$$r = \frac{\sum ((X_i - \bar{X})(Y_i - \bar{Y}))}{\sqrt{\sum (X_i - \bar{X})^2 \sum (Y_i - \bar{Y})^2}} \quad (1)$$

where  $r$  is the value of PCC between any two variables;  $\bar{X}$  and  $\bar{Y}$  are the mean of one variable  $X$  and the other variable  $Y$ . The range of  $r$  is from  $-1$  to  $1$ , where  $0$  means no linear correlation, and a negative or positive value means negative or positive correlation.

### 2.10. ML model setups and evaluation

This study utilizes high-throughput data obtained from experiments, including SSA and permeability as input data, along with BV/TV and the relative expression of osteogenic genes as output data. The schematic diagram of the ML process is depicted in Fig. S1. To increase the diversity of the data and help the model train on different data distributions, thereby improving its generalization ability, we first performed data augmentation. We generated new data points through techniques such as adding feature noise, feature transformation and SMOTE interpolation. Using these methods, the dataset was ultimately augmented to 720 samples. To avoid instability in model training parameters and potential numerical overflow due to varying magnitudes of characteristics, all data were normalized. This normalization facilitates faster convergence of the gradient descent method during model training [24]. Additionally, to capture the nonlinear relationships between original features and enhance the model's fitting capability, high-order polynomial features were generated [25]. This approach enables the model to fit complex decision boundaries, thereby improving classification or regression accuracy. Based on the data characteristics, a Yeo-Johnson transformation was also applied to approximate the nonlinear transformed data to a normal distribution, enhancing the predictive power of the mode [26]. Subsequently, we employed the XGBoost model, a type of gradient boosting regression (GBR) model, to train and predict the importance of material features. This model captures complex nonlinear relationships in the data by constructing multiple decision trees and exhibits strong fitting capabilities, making it highly suitable for nonlinear fitting [20,24]. To optimize model performance, RandomizedSearchCV was used to tune hyperparameters, and k-fold cross-validation was implemented to assess the model and minimize overfitting [27,28]. Model accuracy was evaluated using indices such as  $R^2$ , MAPE, MSE and RMSE [29], which measure the discrepancies between actual and predicted values. Partial dependency plots (PDP) are

tools employed to interpret ML models, particularly tree-based models like random forests and gradient boosting decision trees. PDP can elucidate the correlation between model features and the target, especially highlighting nonlinear relationships.

### 2.11. Statistical analysis

All data were collected from at least three parallel samples for each test and expressed as means  $\pm$  SD, unless otherwise stated in the caption. Data were statistically analyzed using a GraphPad Prism (GraphPad Software, Inc., CA). Student's t-tests or ANOVAs with Tukey's post hoc tests were performed, and the statistical significance was determined as  $P < 0.05$ .

## 3. Results

### 3.1. Characterizations of 3D-printed ceramics

The pictures, micro-CT images and SEM image of CaP ceramics show the macroscopic appearances of 3D-printed sintered ceramic bodies, as shown in Fig. 2A-B, S5. It is found that the geometric structure of CaP Chip and Cyl-scaffold ceramics are intact with no obvious defects and cracks. Fig. 2A shows the arrangement mode of the CaP Chip, this arrangement ensures that structures with the same pore shape are not placed adjacent to each other, thereby enhancing the accuracy of the results. XRD pattern of 3D-printed CaP ceramics is shown in Fig. 2C, and the obtained diffraction peaks were identified by the standard references for Hydroxyapatite (HA) and  $\beta$ -tricalcium phosphate ( $\beta$ -TCP). It showed that printed CaP ceramics were composed of  $\beta$ -TCP and HA without other components, indicating that the modifiers, resins and toners were completely removed without residue left after sintering. The phase composition ratio of HA to  $\beta$ -TCP was 3:7 in formed CaP ceramics. As shown in Fig. 2F, the porosity of the model design is consistent between CaP Chip and Cyl-scaffold. Following 3D printing and sintering, the CaP Cyl-scaffold underwent micro-CT scanning and reconstruction. The porosity of the reconstructed results was calculated and found to be insignificantly different from that of the original model, indicating successful reproduction of the design structures.

Specific surface area (SSA) and permeability of porous ceramic scaffolds are crucial factors influencing osteoinduction. A larger SSA provides more space for cells to attach and proliferate, which facilitates cell growth and differentiation. Additionally, it enhances the adsorption and release of bioactive substances within the body, and accelerates the degradation of CaP ceramics [30]. As demonstrated in Fig. 2E, SSA of both the CaP Chip and Cyl-scaffold exhibits a consistent trend with increasing porosity. The discrepancy in SSA was due to the varied shapes of the structural elements within the samples. Thus, the uniform trend in porosity-related changes in SSA supports the systematic screening of structural designs. The SSA of diamond and polyhedral structures increases with porosity, whereas the trend is less apparent in triangular structures, and remains nearly constant in square structures with porosities of 50 %–70 %. These variations are closely linked to the design of the pore structure and the changes in porosity throughout this study.

The permeability of porous ceramics is related to the efficiency of nutrient and metabolic waste delivery [31]. Appropriate permeability is able to support the formation of new blood vessels, an important step in bone repair, as blood vessels are able to deliver critical nutrients and cells to the scaffold. Fig. 2D shows the permeability of various structural designs. At a lower porosity range (50 %–55 %), the permeability of the triangular and diamond structures is significantly higher compared to the polyhedral and square structures, approximately  $2.5\text{--}3.5 \times 10^{-9} \text{ m}^2$ . However, for the triangular structure with a porosity between 65 % and 75 %, there is no notable difference in permeability. This observation is attributed to the intrinsic characteristics of the triangular structure, suggesting that the influence of porous ceramics with through holes on liquid flow diminishes at higher porosities. In the case of diamond and

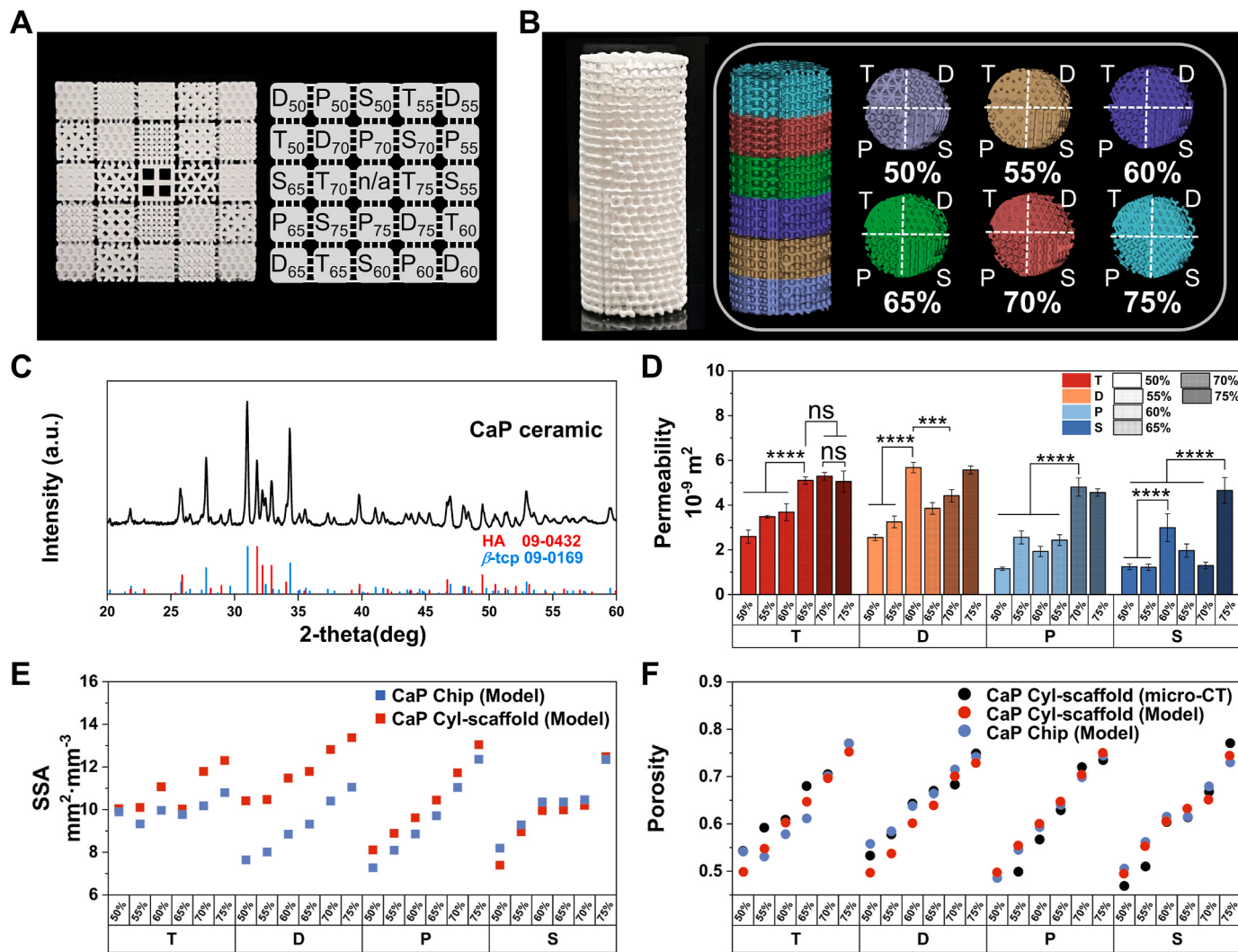


**Fig. 2. Characterization of 3D printing CaP Chip/Cyl-scaffold.** A Picture of CaP Chip and the schematic diagram of 24 structures arrangement. B picture and micro-CT reconstructed images of the CaP Cyl-scaffold. C XRD patterns of 3D-printed CaP ceramics. D Permeability of different structures. (\*\*\*\*: significance level  $P < 0.0001$ ; \*\*\*: significance level  $P < 0.001$ ; \*\*: significance level  $P < 0.01$ ; \*: significance level  $P < 0.05$ ). E Specific surface area and F porosity of different structures.

square structures, a marked increase in permeability is observed at 60 % porosity, indicating that there is a complex connection between permeability and pore structure, which is worthy of future exploration. Anyway, as shown in Table 1, the parameters in this study fall within the

current general study range.

### 3.2. Cell viability and gene expression on CaP chip

To assess the cells grown on CaP Chip with different structures, BMSCs were cocultured with ceramics over the periods of 3, 7, 14 and 21 days. As shown in Fig. 3A, BMSCs grow well on the materials without obvious dead cells and fill the entire CaP Chip volume. After 7days, the cells had completely covered the materials surface and then grew and migrated along the inner surface of the ceramic pit. In the structures with 50 % and 55 % porosity, cells were observed to grow in an inward stack along the periphery of the pore structure. For 60–70 % porosity structures, this phenomenon can be clearly observed in the square groups. After 14 days, cells further migrated and grew along the interior of the pore structure, showed cell growth with a rounded central opening regardless of the original shape. By day 21, almost all pores had been filled with cells.

Fig. 3B shows the cell proliferation in the CaP Chip at different times. After 3 days (Fig. S2), there was no significant difference in cell proliferation rate among the different structures. Higher proliferation rate was observed in the diamond structure with 60 % porosity, polyhedral structure with 50 % and 55 % porosity at days 7. And after 14 days

**Table 1**  
Characteristic parameters of 3D printed CaP Chip/Cyl-scaffold.

Parameter	This study	Reported
Pore geometry		Diamond, Gyroid, Polyhedron-Like, etc. [32–34]
Porosity	50–75 %	50–90 % [35–42]
Model SSA ( $\text{mm}^2 \text{ mm}^{-3}$ )	7.29–13.38	Scaffold: 2.2–8.4 [43–45] Bone: 1.5–11.8 [46,47]
Permeability ( $\times 10^{-9} \text{ m}^2$ )	1.15–5.67	Scaffold: 1–18.7 [40–42,48,49] Bone: $10^{-11}$ – $10^{-8} \text{ m}^2$ [47,50,51]

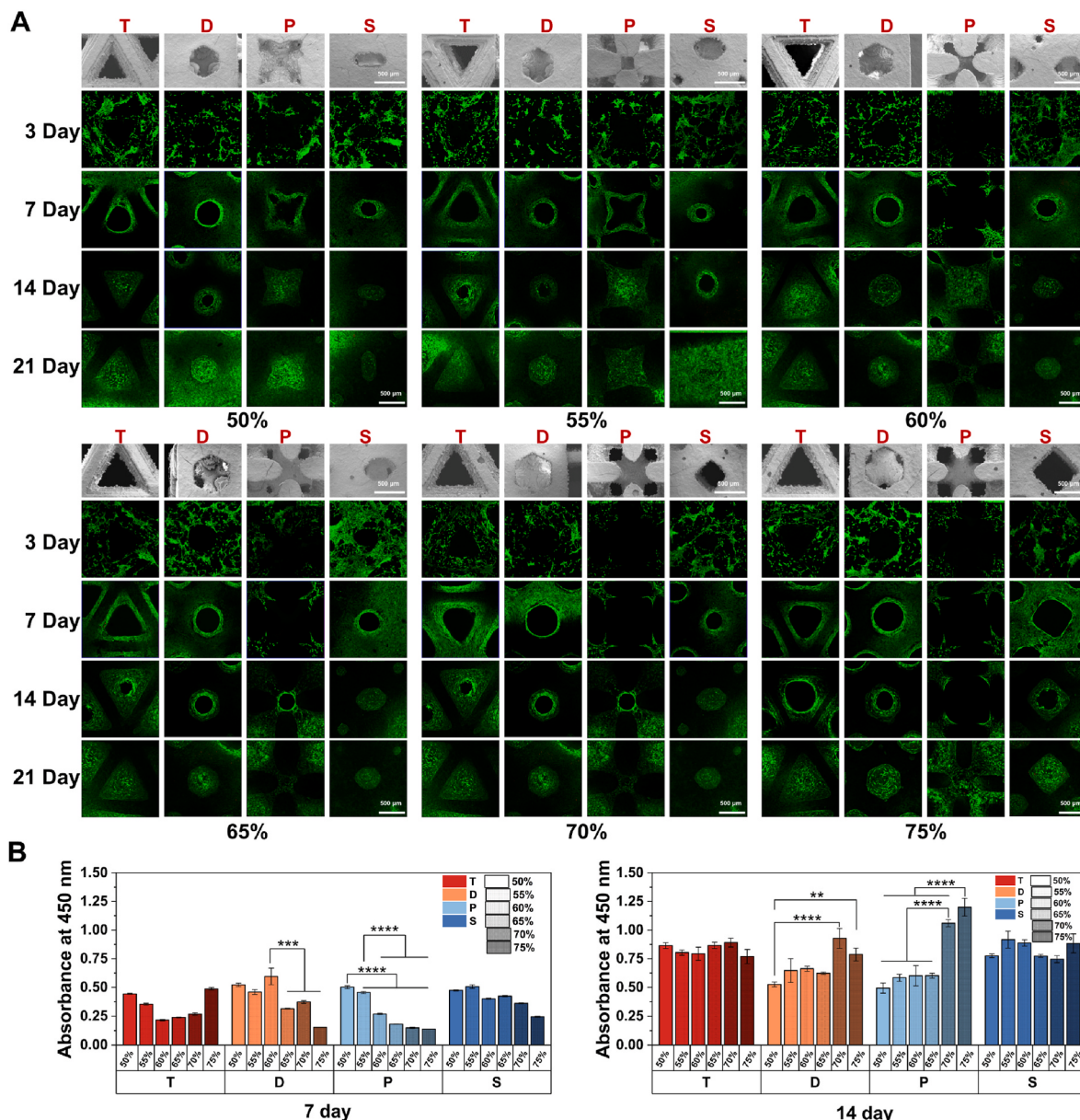


**Fig. 3. In vitro evaluation of CaP Chip.** A CLSM observations for BMSCs growth onto CaP Chip. B CCK-8 results for the proliferation of BMSCs on CaP Chip for 7 and 14 days. (\*\*\*\*: significance level  $P < 0.0001$ ; \*\*\*: significance level  $P < 0.001$ ; \*\*: significance level  $P < 0.01$ ; \*: significance level  $P < 0.05$ ).

culture, in diamond and polyhedral structures, the cell proliferation level of 70 % and 75 % porosity groups was higher than that of others with the same structure.

The effects induced by 24 different structures via CaP Chip on the expression of key osteogenic genes in BMSCs (Fig. S3) were investigated to assess the potential osteogenic ability. The colored heatmap of gene expression, as shown in Fig. 4, Runx-2 and ALP were observed higher expression at 7 and 21 days, respectively. And an elevated COL-I and OPN expression is observed in the polyhedral structure with 65 % porosity and square structure with 70 % porosity after 7 days of coculture. After 14 days of culture, all the groups show prominently upregulated expression of genes. As shown in Fig. 4, the gene expression level of the square structure group is significantly higher than in the other groups after 14 days of coculture.

Unsurprisingly, as reported in the literature, CaP porous ceramics have excellent bioactivity. However, different structures and porosity lead to different cellular behavior on the sample. Notably, in osteogenic gene expression, basic data enumeration may suggest certain trends in

structure-activity relationships, but a more advanced data analysis is needed for deeper insights.

### 3.3. Osteoinductivity evaluation in vivo

In order to explore the ability of the integrated multi-structure CaP ceramics scaffold to induce ectopic osteogenesis *in vivo*, micro-CT was used to reconstruct and analyze the samples. The three-dimensional reconstruction map and quantitative analysis of volume change are shown in Fig. 5, CaP Cyl-scaffold have different degrees of degradation from high porosity to low porosity. As the porosity increases, the degradation between layers gradually increases. In the same porosity, square structure degraded the most, and the degradation of the other three structures was slower (Fig. 5A). The part of CaP Cyl-scaffold with 75 % porosity had disintegrated, so the BV/TV ratio was not analyzed and calculated. In the diamond structure, the porosity had no significant effect BV/TV ratio. As shown in Fig. 5C, the amount of new bone formation is distinguished in all structures. In the polyhedral structure and

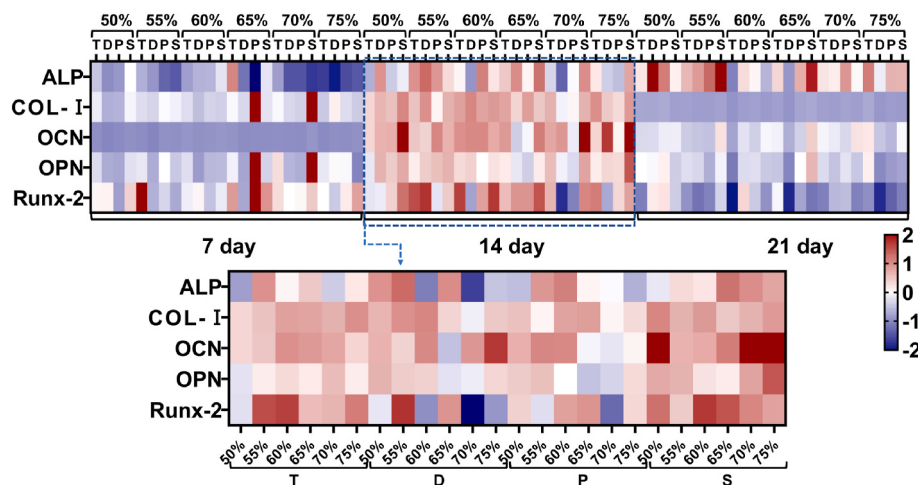


**Fig. 4. Heatmap representation of gene expression.** Blue and red represent low and high expression levels, respectively. All data were calculated as the means. (For interpretation of the references to color in this figure legend, the reader is referred to the Web version of this article.)

the square structure, the BV/TV ratio shows an upward trend with the increase of porosity. The polyhedral structure with 70 % porosity had the largest amount of new bone. The triangular structure with 65 % porosity and the polyhedral structure with 65 % porosity and the square structure with 70 % porosity also showed excellent osteoinductive properties.

Basic histological staining was performed to verify the corresponding osteogenesis results *in vivo*. Results of H&E staining are shown in Fig. 5B. After 180 days of implantation, there are no obvious inflammatory reaction and no fibrous wrapping around the scaffold. The CaP ceramic scaffold is tightly bonded to the tissue, which grows into the pore along the pore wall and gradually fills up. The layer with the highest porosity (75 %) has the extensive degradation, a large number of three-dimensional porous structures are missing, and less bone tissue is observed at this layer. The quantitative analysis of the new bone area is shown in Fig. 5D. CaP Cyl-scaffold with 65–70 % porosity show higher new bone content. Different from the micro-CT results, the structures with the largest new bone area in tissue sections is triangular structure with 70 % porosity. The new bone area of 50 % and 55 % porosity structures is significantly lower than that of other porosity groups. Tissue sections assessed bone growth at the two-dimensional microscopic level, demonstrating the effective osteoinduction and structural-biological property differentiation of CaP porous ceramics. However, since these sections lacked three-dimensional information, CT results were employed as target parameters for establishing SAR in subsequent analyses.

#### 3.4. Correlation between the structural parameters and osteoinductivity

After conducting *in vivo* and *in vitro* experiments, we aimed to explore the SAR between the structural parameters of the ceramics and their impact on cell proliferation, differentiation and osteoinductivity. To this end, we analyzed the data using the Pearson correlation coefficient (PCC) and visualized the results in a heat map, as shown in Fig. 6. The PCC between BV/TV and the porosity of the ceramic was 0.541 ( $P < 0.05$ ), indicating a positive correlation between these variables. However, no significant linear relationship was found between different macroporous structures and BV/TV. The *in vitro* proliferation of BMSCs (CCK8) initially showed a negative correlation with the porosity and SSA of the ceramic. However, over time, this relationship became positive, aligning with the cell proliferation observed on the ceramic surfaces. Additionally, the figure demonstrates that the expression of osteogenic genes in BMSCs does not exhibit a significant linear correlation with the porosity, SSA, permeability, or macroporous structure of the ceramics. Therefore, the search for nonlinear relations may provide more valuable

information.

#### 3.5. Machine learning and nonlinear fitting

According to the PCC, some data displayed no significant linear relationships. To further explore these data, an XGBoost model (Fig. 7A) was employed to attempt fitting the nonlinear relationships between material characteristics (SSA, permeability) and osteogenic properties (BV/TV, osteogenic gene expression). To avoid overfitting on limited training datasets due to the strong learning capabilities of ML models and to ensure reliable evaluation of prediction accuracy, we use K-fold cross-validation to assess model performance, as Fig. 7B shown. In K-fold cross-validation, the data set is evenly divided into 5 subsets, 4 of which are used for training at a time, and the remaining subset is used as the test set. In ML,  $R^2$ , MAPE, MSE and RMSE are parameters used to evaluate the prediction accuracy of models. A higher  $R^2$  value, closer to 1, and lower values of MSE, MAPE and RMSE indicate more accurate predictions and better model performance. As demonstrated in Table S2 and Fig. S4, this model exhibits excellent performance. Fig. 7C-D shows partial dependency plots (PDP) that illustrate the dependency of osteogenesis performance on material characteristics, revealing nonlinear relationships presented in the PCC results. The plot shows a trend where BV/TV initially increases with SSA but then declines, in which a platform appeared at the position of SSA ranging 9.66–11.73  $\text{mm}^2 \text{mm}^{-3}$ , indicating that SSA in this area can promote the formation of new bone. The PDP also indicates that the expressions of COL-I, OCN, OPN and Runx-2 genes exhibit a trend of increase-plateau-decline as SSA increases. Specifically, the plateau for COL-I occurs between 9.91 and 10.69  $\text{mm}^2 \text{mm}^{-3}$ , the plateau for OCN is between 10.49 and 10.69, the plateau for OPN is between 9.91 and 10.69  $\text{mm}^2 \text{mm}^{-3}$ , and the plateau for Runx-2 gene expression appears between 9.34 and 9.72  $\text{mm}^2 \text{mm}^{-3}$ . ALP gene expression reaches its peak at an SSA of 9.817  $\text{mm}^2 \text{mm}^{-3}$ , followed by a decline and a plateau phase. These correlations collectively shape the relationship between SSA and BV/TV, aligning with the fitting patterns. However, there is no apparent regularity in the relationship between material permeability and BV/TV. Notably, the expressions of osteogenic genes COL-I, OPN, and OCN show a peak at a permeability of  $3.74 \times 10^{-9} \text{ m}^2$ . Meanwhile, ALP expression increases with increasing permeability. Runx-2 expression shows no significant change with varying permeability. The expression of different genes reflects the osteogenic differentiation of cells at various stages, providing new insights into the molecular mechanisms of osteoinduction.

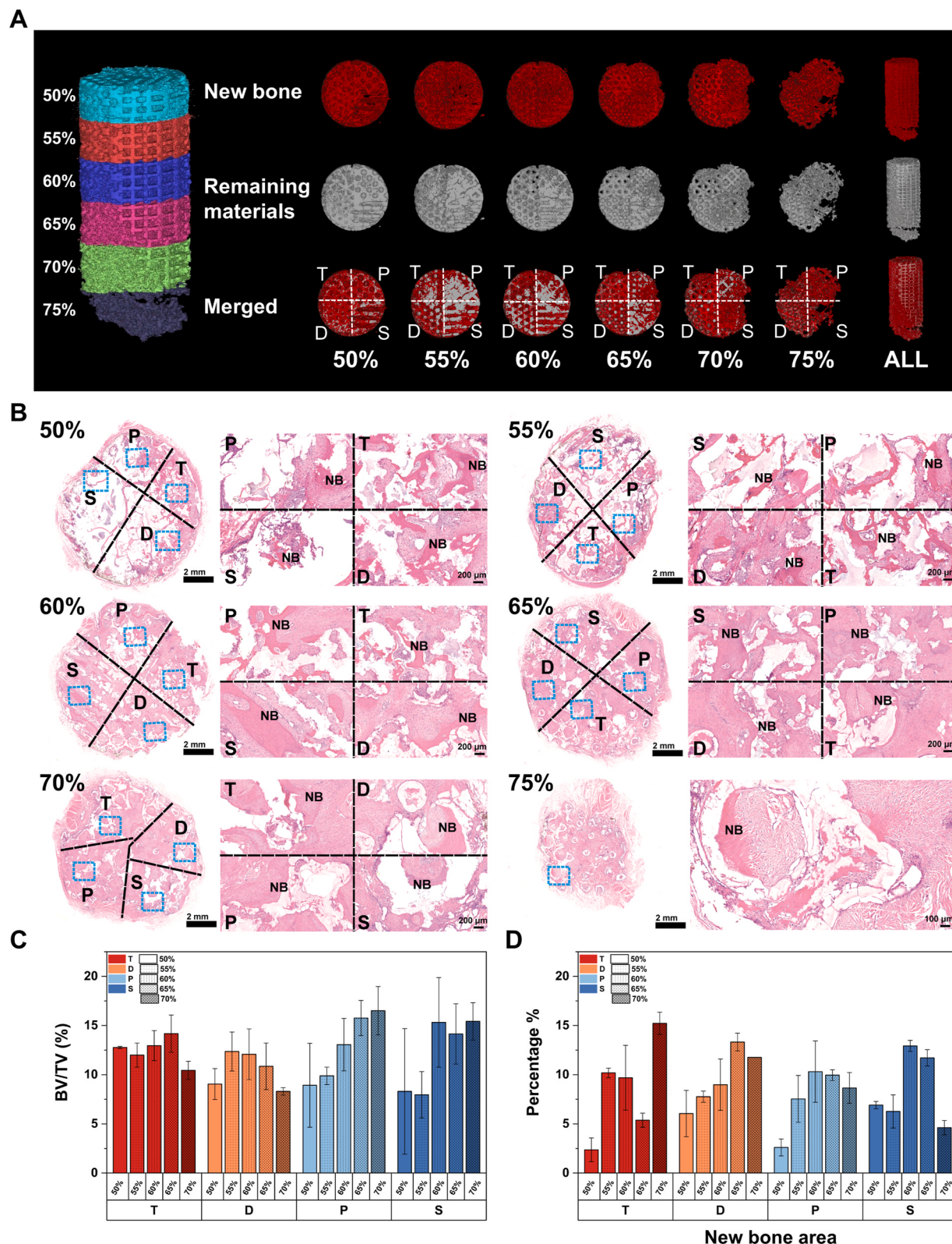


**Fig. 5. In vivo evaluation of the CaP Cyl-scaffold.** A Evaluation of the formation of new bone on the CaP Cyl-scaffold by 3D reconstruction after micro-CT scanning. B Histological assessment of neo-bone formation (NB, new bone tissue). C Quantification of the new bone volume to tissue volume ratio (BV/TV), all the samples show no statistically significant differences (NS). D Quantitative analysis of new bone tissue area at each layer structure of the CaP Cyl-scaffold, all the samples show no statistically significant differences (NS).

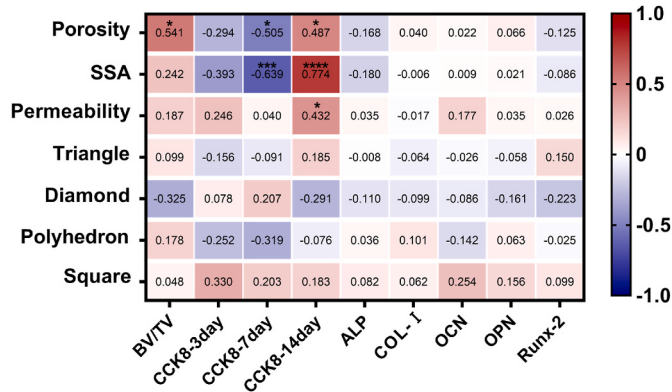


**Fig. 6. Pearson correlation coefficients matrix between inputs and outputs, expressing a positive or negative linear relationship (\*\*\*\*: significance level  $P < 0.0001$ ; \*\*\*: significance level  $P < 0.001$ ; \*\*: significance level  $P < 0.01$ ; \*: significance level  $P < 0.05$ ).**

#### 4. Discussion

High-throughput techniques such as polymer templating, metal etching and single-cell studies, have been extensively utilized in biomedical research. The application of these techniques in ceramics were rarely reported, often primarily focusing on the composition ratios of ceramic components. The osteoinductive properties of BCP ceramics are influenced by factors such as structural design, surface morphology and active ions [52–55]. Numerous studies have documented the effects

of pore shape and porosity on CaP ceramics [56,57]. However, traditional cultivation methods lack efficiency and do not allow for the isolated observation of scaffold structure effects without the confounding influences of surface area and ion release concentration. Given the intertwined nature of BCP ceramic properties, where alterations in one feature inevitably affect others, it is challenging to assess the impact of individual material properties on the osteoinduction using conventional synthesis and processing techniques. Therefore, designing ceramic samples that is not only efficient but also capable of isolating and studying the effects of individual factors on osteoinduction is necessary. These intricately designed scaffolds minimize the interference and errors associated with other variables in traditional experiments, enabling a focused analysis on the effects of pore structures on the osteoinductivity of the ceramics. Combined with 3D printing and high-throughput technologies would significantly improve the efficiency of key factor screening, and also efficiently promote the application of CaP ceramics. The potential of high-throughput screening lies in its ability to screen thousands of scaffold designs, including variations in chemical composition, porosity, pore geometry and even 3D shapes. The advantage of high-throughput screening is that it can rapidly assess a large number of parameters simultaneously, identifying the optimal combinations of factors that improve osteoinductive properties. Furthermore, the combination of high-throughput screening with ML significantly accelerates the exploration of material properties and biological performance. This study executed high-throughput screening of scaffold structures based on CaP ceramics. The 24 structures included in this work encompass the most common features of osteoinductive CaP ceramics and the critical factors emphasized in the literature, and our results indicate that they

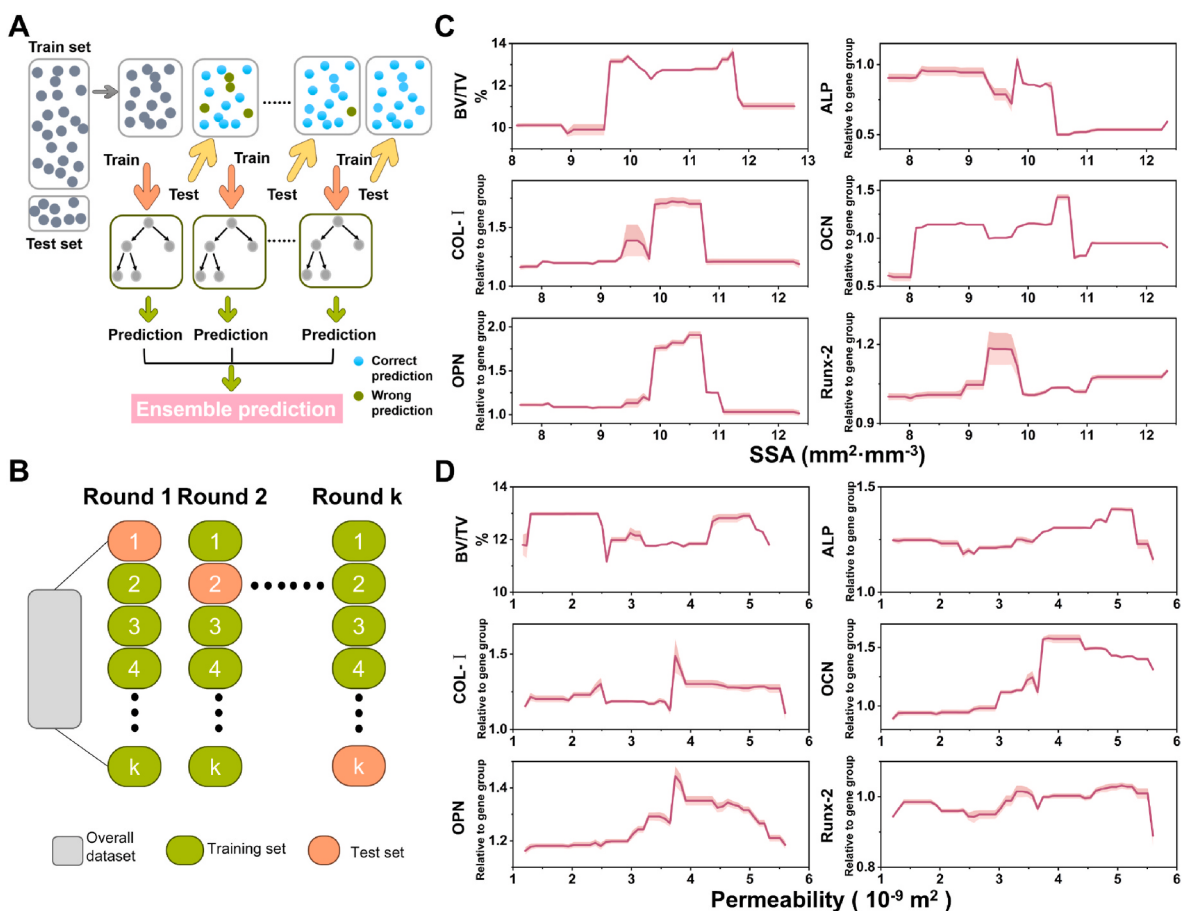


**Fig. 7. XGBoost model performance of nonlinear fitting between material characteristics and osteogenic properties. A** Flow diagram of XGBoost machine learning method. **B** K-fold cross-validation was utilized to estimate the model prediction accuracy. The partial dependence plots of **C** SSA and **D** permeability VS BV/TV and expressions of osteogenic genes.

provide robust design parameters for CaP bioceramic scaffolds. CaP Chip and CaP Cyl-scaffold were used to evaluate *in vitro* cell responses (that is early-stage biological responses i.e., cell adhesion, spreading, and proliferation) and *in vivo* long-term biological responses, respectively. Two different stacks of 3D units with the same 24 structures allowed us to ensure the consistency of the scaffold dimensions in the same evaluation system. Although not randomized in a strict statistical sense, this approach draws on well-documented experimental phenomena and therefore limits bias by encompassing a wide range of realistic scaffold factors. Furthermore, we are developing a data-driven method to identify common structural parameters—such as curvature, SSA, permeability and overall porosity—that extend beyond specific scaffold geometries. While we acknowledge that some specialized porous or non-porous designs (e.g., Gyroid, hexagonal close-packed spheres, flow-channel structures) were not included in the current investigation, we plan to incorporate these and other architectures in future high-throughput screening efforts for osteoinductive biomaterials. In future studies, extending the diversification of structure unit in three-dimensional space and increasing the sample size will offer stronger data support and expand the exploration of the design space.

Based on previous studies, the influence of pore geometry on the osteogenic properties of CaP ceramics stems primarily from how different pore geometries affect cell adhesion, spreading and osteogenic differentiation. It is reported that the growth rate of the cells is significantly affected by the 3D pore geometry of the substrate material [58]. Due to the influence of cytoskeleton force, concave spherical surface is more suitable for cell migration than flat or convex spherical surface, and the higher the curvature of pores, the more conducive to cell or tissue growth [59–63]. In our study, the spreading of BMSCs on the CaP Chip (Fig. 3A) follows changes in the curvature of the pore, the triangular and polyhedral structures, which feature areas of large curvature, may induce eddy currents during liquid flow. The formation of these eddy currents can facilitate the deposition of cells and substances, causing cells to accumulate and gradually form spherical tissues that grow inward until the pores are filled [64]. However, results from the CCK-8 assay (Fig. 3B) indicated no significant difference in cell viability between groups with different pore geometries. Nonetheless, in the diamond and polyhedral structures, variations in porosity influenced cell proliferation levels at different time points. While previous studies have acknowledged the impact of pore structure on osteogenic differentiation, the specific relationship between pore diameter, rod diameter, porosity, pore geometry and osteogenic differentiation was not clearly discernible due to the use of independent structures by researchers. The design of CaP Chip/Cyl-scaffold in this study focusses on the relationship between porosity, pore geometry and osteoinduction. The results from qRT-PCR suggested that pore geometry had a modest effect on the osteogenic differentiation of BMSCs, though this effect was not pronounced. Heat map analysis of gene expression revealed that the square structure exhibited relatively higher gene expression at 14 days, suggesting that the macroscopic pore does not strongly influence cellular differentiation. This finding highlights the nuanced role of pore geometry in modulating the osteogenic potential of CaP ceramics. While pore geometry has a limited effect on osteoinduction under comparable SSA and porosity conditions, it significantly impacts the scaffold's mechanical properties, which is why many studies prioritize optimizing mechanical traits through pore geometry [34].

CaP ceramics with porous structure demonstrate significant osteoinductive capabilities *in vivo*, which are attributed not only to the chemical properties of the CaP ceramics but also to the optimal porosity that provides a conducive environment for bone tissue growth. Various levels of porosity influence protein adsorption, ion exchange and apatite formation. Micro-CT imaging revealed that structures with 50 %–70 % porosity remained largely intact after 180 days of implantation, with new bone formation observed in all configurations. Notably, the polyhedral structure with 70 % porosity exhibited the most substantial new bone growth, indicating its superior efficacy in inducing bone formation.

However, structures with a porosity of 75 % showed significant disintegration due to the degradation of the CaP ceramics *in vivo*, suggesting that higher porosity and larger pore sizes lead to increased degradation. This degradation pattern impacts the internal porous network and mechanical strength of the bioceramic scaffolds. Matching the degradation rate with the osteogenic rate is crucial, as the release of CaP ions during degradation can influence osteogenesis and angiogenesis, ultimately affecting the outcomes of *in situ* bone regeneration and osseointegration [30].

Then, the correlation between pore structure parameters and the outcomes of *in vitro* and *in vivo* experiments was analyzed using the PCC, aiming to identify the key factors influencing osteogenic induction in porous ceramics through structure-activity analysis. The analysis revealed that porosity was significantly positively correlated with new bone formation (Fig. 6). Appropriate porosity is crucial not only for the overall mechanical strength of the material but also for cell attachment, migration and proliferation on the material's surface. These results further confirmed the lack of a significant linear correlation between pore geometry and new bone formation or cell proliferation and differentiation. We hypothesize that this outcome is due to the complex interplay of various structural parameters such as SSA, permeability and curvature, which are influenced by different pore geometry and collectively affect bone formation and cellular behavior. ML was employed to model the correlation between osteogenic performance outcomes observed in the experiment and both SSA and permeability. Analysis of PDP reveals that the relationship between SSA and BV/TV initially increases and then decreases. This pattern may result from varying degradation rates of materials influenced by different SSA following scaffold implantation [7]. Regarding the correlation between the expression of osteogenic genes, SSA and permeability, it is noted that gene expression peaks when SSA is  $10.49\text{--}10.69 \text{ mm}^2 \text{ mm}^{-3}$  and permeability is  $3.74 \times 10^{-9} \text{ m}^2$ . These findings indicated that these parameters significantly benefited the osteogenic differentiation. As shown in Table 1, previous studies indicate that the SSA of biological scaffolds typically ranges between 2.2 and  $8.4 \text{ mm}^2 \text{ mm}^{-3}$ , while human bone SSA, measured via micro-CT scans, is approximately  $1.5\text{--}11.8 \text{ mm}^2 \text{ mm}^{-3}$  [46,47], which is a wide range. This study identifies an optimal SSA range of  $10.49\text{--}10.69 \text{ mm}^2 \text{ mm}^{-3}$ , which is deemed suitable for our purposes. A larger SSA not only enhances cell attachment and proliferation but is also associated with a higher porosity, crucial for the effective diffusion of nutrients, metabolites and wastes, supporting the osteoinductivity of CaP ceramics [65]. Additionally, higher porosity facilitates the passage of supplements and aids in waste removal, although it may negatively impact cell attachment and the mechanical properties of the scaffold [66]. Conversely, smaller pore sizes or lower porosity have higher density, providing enhanced mechanical properties and lower permeability [45,67–69]. In Fig. 2, the permeability of porous scaffolds generally increases with porosity [70]. Cellular nutrition and oxygenation depend on diffusion prior to angiogenesis. The extent and speed of mass transfer through diffusion are dictated by the permeability of the porous biomaterial [50]. If high pressure or concentration gradients are required to transport nutrients and oxygen to cells deep within the scaffold, cellular metabolism in internal areas may likely be compromised, hindering tissue growth in and regeneration [71]. Therefore, appropriate permeability is crucial for ensuring unimpeded mass transport within the scaffold to maximize its bone regenerative performance. This study determines an optimal permeability rate of  $3.74 \times 10^{-9} \text{ m}^2$ , which also aligns with the permeability ranges of human bone. Additionally, given the wide variability in human bone permeability, the optimal value derived from this study provides significant guidance for future design of biomaterial scaffolds. A review of the pore structure revealed that these parameters corresponded with 65 % porosity in square and diamond structures and 70 % porosity in polyhedral structures. According to the BV/TV results, these configurations performed exceptionally well for new bone formation *in vivo*. This relationship will provide valuable insights for future design

considerations of pore structures.

In this study, we focused on how the structural factors of CaP ceramics influence osteoinductivity, (e.g., composition, surface characteristics, mechanical properties). Which was objectively limited by the available *in vivo* and *in vitro* characterization methods for bioceramics scaffolds. It also offers valuable insights into the impact of porosity and pore geometry on osteoinduction. Moving forward, it's worthy to expand high-throughput screening approach to a broader range of biomaterials [13,72–74], such as polymers, metals and composites, and more factors (like surface and mechanical properties [75–78]) in order to fully explore this method's potential. By investigating multiple material systems, we can identify universal design principles applicable across different biomaterials, thereby enhancing the versatility and application of high-throughput screening in tissue engineering.

The integration of AI-driven design tools and computer-aided optimization methods can significantly enhance the design process. It is now possible to achieve rapid and rigorous screening of biomaterials through the integration of experiments, simulations and ML [79]. ML algorithms can predict the performance of the scaffold based on different input parameters, reducing the need for cumbersome and expensive trial-and-error experiments [80]. In addition, the computational design platform can quickly iterate the scaffold structure, making the exploration of design space more efficient. By integrating AI and computing technologies into the scaffold design process, we can accelerate the development of optimal scaffolds specifically tailored for multiple applications such as bone regeneration.

## 5. Conclusions

In summary, we performed a high-throughput screening of osteoinductive factors. CaP ceramic integrated 24 different pore structures were fabricated by DLP-3D printing, which to evaluate the osteoinductive effect of CaP ceramics. This integration facilitates both *in vitro* and *in vivo* experiments, allowing for effective evaluation of osteoinductivity based solely on variations in pore structure. It not only saves experimental time but also reduces the number of animals needed for the study. Experimental screening revealed that the polyhedral structure with a porosity of 70 % had the highest rate of new bone formation. Analysis of material properties using PCC as well as ML revealed multiple correlations between structural parameters and osteoinductivity, cell proliferation and differentiation, confirming that new bone formation in CaP porous ceramics is largely affected by porosity and SSA, with pore geometry having minimal impact. The results also indicated that a porous structure with an SSA of 10.49–10.69 mm<sup>2</sup> mm<sup>-3</sup> and a permeability of  $3.74 \times 10^{-9}$  m<sup>2</sup> promotes osteogenic differentiation, and the structure corresponding to these parameters also performed well in new bone formation *in vivo*, which provided valuable insights for future studies of the osteoinductive biomaterials. The high-throughput screening and ML data analysis developed in this study would expedite the identification of key factors and parameter acquisition, serving as an efficient method for advancing other tissue regenerative biomaterials.

## CRediT authorship contribution statement

**Yunyi Liu:** Writing – review & editing, Writing – original draft, Validation, Software, Methodology, Investigation, Formal analysis, Data curation, Conceptualization. **Quanle Cao:** Methodology, Data curation. **Shengyi Yong:** Software, Methodology, Investigation, Formal analysis, Data curation. **Jing Wang:** Methodology, Investigation. **Xuening Chen:** Methodology, Investigation, Formal analysis. **Yumei Xiao:** Methodology, Investigation. **Jiangli Lin:** Validation, Software, Formal analysis. **Mingli Yang:** Validation, Software, Formal analysis. **Kefeng Wang:** Writing – review & editing, Supervision, Methodology, Investigation. **Xiangfeng Li:** Writing – review & editing, Supervision, Methodology. **Xiangdong Zhu:** Writing – review & editing, Supervision, Investigation, Funding acquisition. **Xingdong Zhang:** Supervision, Methodology,

Conceptualization.

## Funding

We gratefully acknowledge the financial support of National Natural Science Foundation of China (52172284) and National Key Research and Development Program of China (2022YFC2401801, 2021YFB3802105).

## Declaration of competing interest

The authors declare that they have no known competing financial interests or personal relationships that could have appeared to influence the work reported in this paper.

## Acknowledgments

We thank Jiao Lu, Lingzhu Yu and Guolong Meng for in the help with SEM and CLSM characterization. We thank Dr. Chengxin He from National Engineering Research Center for Biomaterials of Sichuan University for his guidance on Machine Learning. We also thank Dr. Li Chen from the Analytical & Testing Center of Sichuan University for her help with Micro-CT.

## Appendix A. Supplementary data

Supplementary data to this article can be found online at <https://doi.org/10.1016/j.biomaterials.2025.123348>.

## Data availability

Data will be made available on request.

## References

- [1] I. Dumic-Cule, M. Pecina, M. Jelic, M. Jankolija, I. Popek, L. Grgurevic, S. Vukicevic, Biological aspects of segmental bone defects management, Int. Orthop. 39 (2015) 1005–1011, <https://doi.org/10.1007/s0264-015-2728-4>.
- [2] J. Chang, X. Zhang, K. Dai, Chapter 1 - material characteristics, surface/interface, and biological effects on the osteogenesis of bioactive materials, in: J. Chang, X. Zhang, K. Dai (Eds.), B.T.-B.M. for B.R., Academic Press, 2020, pp. 1–103, <https://doi.org/10.1016/B978-0-12-813503-7.00001-7>.
- [3] Z. Tang, X. Li, Y. Tan, H. Fan, X. Zhang, The material and biological characteristics of osteoinductive calcium phosphate ceramics, Regen. Biomater. 5 (2018) 43–59, <https://doi.org/10.1093/rb/rbx024>.
- [4] P. Feng, R. Zhao, W. Tang, F. Yang, H. Tian, S. Peng, H. Pan, C. Shuai, Structural and functional adaptive artificial bone: materials, fabrications, and properties, Adv. Funct. Mater. (2023) 2214726, <https://doi.org/10.1002/adfm.202214726>.
- [5] P. Diloksumpan, R.V. Bolanos, S. Cokelaere, B. Pouran, J. Grauw, M. Rijen, R. Weeren, R. Levato, J. Malda, Orthotopic bone regeneration within 3D printed bioceramic scaffolds with region-dependent porosity gradients in an equine model, Adv. Healthcare Mater. 9 (2020) 1901807, <https://doi.org/10.1002/adhm.201901807>.
- [6] T.-R. Kim, T.S. Goh, J.S. Lee, D. Ryu, S.-Y. Yoon, C. Lee, Experimental and numerical investigations for compressive behavior of porous hydroxyapatite bone scaffold fabricated via freeze-gel casting method, Mater. Des. 231 (2023) 112080, <https://doi.org/10.1016/j.matdes.2023.112080>.
- [7] F. Shi, X. Fang, T. Zhou, X. Huang, K. Duan, J. Wang, S. Qu, W. Zhi, J. Weng, Macropore regulation of hydroxyapatite osteoinduction via microfluidic Pathway, Indian J. Manag. Sci. 23 (2022) 11459, <https://doi.org/10.3390/ijms231911459>.
- [8] Y. Wu, P. Liu, C. Feng, Q. Cao, X. Xu, Y. Liu, X. Li, X. Zhu, X. Zhang, 3D printing calcium phosphate ceramics with high osteoinductivity through pore architecture optimization, Acta Biomater. 185 (2024) 111–125, <https://doi.org/10.1016/j.actbio.2024.07.008>.
- [9] M.J. Zafar, D. Zhu, Z. Zhang, 3D printing of bioceramics for bone tissue engineering, Materials 12 (2019), <https://doi.org/10.3390/ma12203361> (Basel, Switzerland).
- [10] J. Wang, Y. Tang, Q. Cao, Y. Wu, Y. Wang, B. Yuan, X. Li, Y. Zhou, X. Chen, X. Zhu, C. Tu, X. Zhang, Fabrication and biological evaluation of 3D-printed calcium phosphate ceramic scaffolds with distinct macroporous geometries through digital light processing technology, Regen. Biomater. 9 (2022), <https://doi.org/10.1093/rb/rbac005>.
- [11] R. Macarron, M.N. Banks, D. Bojanic, D.J. Burns, D.A. Cirovic, T. Garyantes, D.V. S. Green, R.P. Hertzberg, W.P. Janzen, J.W. Paslay, U. Schopfer, G.S. Sittampalam,

- Impact of high-throughput screening in biomedical research, *Nat. Rev. Drug Discov.* 10 (2011) 188–195, <https://doi.org/10.1038/nrd3368>.
- [12] F. Soheilmoghaddam, M. Rumble, J. Cooper-White, High-throughput routes to biomaterials discovery, *Chem. Rev.* 121 (2021) 10792–10864, <https://doi.org/10.1021/acs.chemrev.0c01026>.
- [13] T.A.B. van der Boon, L. Yang, L. Li, D.E. Córdova Galván, Q. Zhou, J. de Boer, P. van Rijn, Well plate integrated topography gradient screening technology for studying cell-surface topography interactions, *Adv. Biosyst.* 4 (2020), <https://doi.org/10.1002/adbi.201900218>.
- [14] M.B. Oliveira, M.P. Ribeiro, S.P. Miguel, A.I. Neto, P. Coutinho, I.J. Correia, J. F. Mano, In vivo high-content evaluation of three-dimensional scaffolds biocompatibility, *Tissue Eng. C Methods* 20 (2014) 851–864, <https://doi.org/10.1089/ten.tec.2013.0738>.
- [15] B. Peng, Y. Wei, Y. Qin, J. Dai, Y. Li, A. Liu, Y. Tian, L. Han, Y. Zheng, P. Wen, Machine learning-enabled constrained multi-objective design of architected materials, *Nat. Commun.* 14 (2023) 6630, <https://doi.org/10.1038/s41467-023-42415-y>.
- [16] Q.-Y. Cai, L.-Z. Qiao, S.-J. Yao, D.-Q. Lin, Machine learning assisted QSAR analysis to predict protein adsorption capacities on mixed-mode resins, *Separation and Purification Technology* 340 (2024) 126762, <https://doi.org/10.1016/j.seppur.2024.126762>.
- [17] Y. Guyot, I. Papantoniou, Y.C. Chai, S. Van Bael, J. Schrooten, L. Geris, A computational model for cell/ECM growth on 3D surfaces using the level set method: a bone tissue engineering case study, *Biomech. Model. Mechanobiol.* 13 (2014) 1361–1371, <https://doi.org/10.1007/s10237-014-0577-5>.
- [18] S. Horikawa, K. Suzuki, K. Motojima, K. Nakano, M. Nagaya, H. Nagashima, H. Kaneko, M. Aizawa, Material design of porous hydroxyapatite ceramics via inverse analysis of an estimation model for bone-forming ability based on machine learning and experimental validation of biological hard tissue responses, *Materials* 17 (2024) 571, <https://doi.org/10.3390/ma17030571>.
- [19] B. Chen, J. Dong, M. Ruelas, X. Ye, J. He, R. Yao, Y. Fu, Y. Liu, J. Hu, T. Wu, C. Zhou, Y. Li, L. Huang, Y.S. Zhang, J. Zhou, Artificial intelligence-assisted high-throughput screening of printing conditions of hydrogel architectures for accelerated diabetic wound healing, *Adv. Funct. Mater.* 32 (2022) 2201843, <https://doi.org/10.1002/adfm.202201843>.
- [20] S. Lin, Y. Zhuang, K. Chen, J. Lu, K. Wang, L. Han, M. Li, X. Li, X. Zhu, M. Yang, G. Yin, J. Lin, X. Zhang, Osteoinductive biomaterials: machine learning for prediction and interpretation, *Acta Biomater.* 187 (2024) 422–433, <https://doi.org/10.1016/j.actbio.2024.08.017>.
- [21] J.-C. Huang, Y.-C. Tsai, P.-Y. Wu, Y.-H. Lien, C.-Y. Chien, C.-F. Kuo, J.-F. Hung, S.-C. Chen, C.-H. Kuo, Predictive modeling of blood pressure during hemodialysis: a comparison of linear model, random forest, support vector regression, XGBoost, LASSO regression and ensemble method, *Comput. Methods Progr. Biomed.* 195 (2020) 105536, <https://doi.org/10.1016/j.cmpb.2020.105536>.
- [22] A. Ogunleye, Q.-G. Wang, XGBoost model for chronic kidney disease diagnosis, *IEEE ACM Trans. Comput. Biol. Bioinf.* 17 (2020) 2131–2140, <https://doi.org/10.1109/TCBB.2019.2911071>.
- [23] X.-Y. Zhang, G. Fang, S. Leeflang, A.A. Zadpoor, J. Zhou, Topological design, permeability and mechanical behavior of additively manufactured functionally graded porous metallic biomaterials, *Acta Biomater.* 84 (2019) 437–452, <https://doi.org/10.1016/j.actbio.2018.12.013>.
- [24] H. Li, Z. Ai, L. Yang, W. Zhang, Z. Yang, H. Peng, L. Leng, Machine learning assisted predicting and engineering specific surface area and total pore volume of biochar, *Bioresour. Technol.* 369 (2023) 128417, <https://doi.org/10.1016/j.biotech.2022.128417>.
- [25] J. Heaton, An empirical analysis of feature engineering for predictive modeling, in: *SoutheastCon*, 2016, 2016, pp. 1–6, <https://doi.org/10.1109/SECON.2016.7506650>.
- [26] M. Abbas, Y. El-Manzalawy, Machine learning based refined differential gene expression analysis of pediatric sepsis, *BMC Med. Genom.* 13 (2020) 122, <https://doi.org/10.1186/s12920-020-00771-4>.
- [27] S. Saud, B. Jamil, Y. Upadhyay, K. Irshad, Performance improvement of empirical models for estimation of global solar radiation in India: a k-fold cross-validation approach, *Sustain. Energy Technol. Assessments* 40 (2020) 100768, <https://doi.org/10.1016/j.seta.2020.100768>.
- [28] L. Yang, A. Shami, On hyperparameter optimization of machine learning algorithms: theory and practice, *Neurocomputing* 415 (2020) 295–316, <https://doi.org/10.1016/j.neucom.2020.07.061>.
- [29] Y. Shi, J. Wang, Q. Wang, Q. Jia, F. Yan, Z.-H. Luo, Y.-N. Zhou, Supervised machine learning algorithms for predicting rate constants of ozone reaction with micropollutants, *Ind. Eng. Chem. Res.* 61 (2022) 8359–8367, <https://doi.org/10.1021/acs.iecr.1c04697>.
- [30] A. Diez-Escudero, M. Espanol, S. Beats, M.-P. Ginebra, *In vitro* degradation of calcium phosphates: effect of multiscale porosity, textural properties and composition, *Acta Biomater.* 60 (2017) 81–92, <https://doi.org/10.1016/j.actbio.2017.07.033>.
- [31] M.R. Dias, P.R. Fernandes, J.M. Guedes, S.J. Hollister, Permeability analysis of scaffolds for bone tissue engineering, *J. Biomech.* 45 (2012) 938–944, <https://doi.org/10.1016/j.jbiomech.2012.01.019>.
- [32] H. Zhang, M. Zhang, D. Zhai, C. Qin, Y. Wang, J. Ma, H. Zhuang, Z. Shi, L. Wang, C. Wu, Polyhedron-like biomaterials for innervated and vascularized bone regeneration, *Adv. Mater.* 35 (2023) 2302716, <https://doi.org/10.1002/adma.202302716>.
- [33] Q. Lu, J. Diao, Y. Wang, J. Feng, F. Zeng, Y. Yang, Y. Kuang, N. Zhao, Y. Wang, 3D printed pore morphology mediates bone marrow stem cell behaviors via RhoA/ROCK2 signaling pathway for accelerating bone regeneration, *Bioact. Mater.* 26 (2023) 413–424, <https://doi.org/10.1016/j.bioactmat.2023.02.025>.
- [34] Q. Zhang, L. Ma, X. Ji, Y. He, Y. Cui, X. Liu, C. Xuan, Z. Wang, W. Yang, M. Chai, X. Shi, High-strength hydroxyapatite scaffolds with minimal surface macrostructures for load-bearing bone regeneration, *Adv. Funct. Mater.* 32 (2022) 2204182, <https://doi.org/10.1002/adfm.202204182>.
- [35] P. Hameed, C.-F. Liu, R. Ummethala, N. Singh, H.-H. Huang, G. Manivasagam, K. G. Prashanth, Biomorphic porous Ti6Al4V gyroid scaffolds for bone implant applications fabricated by selective laser melting, *Prog. Addit. Manuf.* 6 (2021) 455–469, <https://doi.org/10.1007/s04964-021-00210-5>.
- [36] G.A. Macheras, S.D. Koutsostathis, S.P. Galanakos, Cementless fully porous-coated implant-bone interface in revision total hip arthroplasty, in: T. Karachalias (Ed.), *Bone-Implant Interface in Orthopedic Surgery: Basic Science to Clinical Applications*, Springer, London, 2014, pp. 169–182, [https://doi.org/10.1007/978-1-4471-5409-9\\_13](https://doi.org/10.1007/978-1-4471-5409-9_13).
- [37] D. Mahmoud, M.A. Elbestawi, Selective laser melting of porosity graded lattice structures for bone implants, *Int. J. Adv. Manuf. Technol.* 100 (2019) 2915–2927, <https://doi.org/10.1007/s00170-018-2886-9>.
- [38] M.A. Noordin, M.I. Kori, A.H. Abdul Wahab, A. Syahrom, A.P. Md Saad, Fluid flow analysis of integrated porous bone scaffold and cancellous bone at different skeletal sites: *in silico* study, *Transport Porous Media* 145 (2022) 271–290, <https://doi.org/10.1007/s11242-022-01849-6>.
- [39] F. Deng, L. Liu, Z. Li, J. Liu, 3D printed Ti6Al4V bone scaffolds with different pore structure effects on bone ingrowth, *J. Biol. Eng.* 15 (2021) 4, <https://doi.org/10.1186/s13036-021-00255-8>.
- [40] R. Paul, M. Rana, A. Gupta, T. Banerjee, S. Kumar Karmakar, A. Roy Chowdhury, Design of biomimetic porous scaffolds for bone tissue engineering, *Transport Porous Media* 151 (2024) 1453–1473, <https://doi.org/10.1007/s11242-024-02082-z>.
- [41] M. Bahraminasab, Challenges on optimization of 3D-printed bone scaffolds, *Biomed. Eng. Online* 19 (2020) 69, <https://doi.org/10.1186/s12938-020-00810-2>.
- [42] A.A. Acar, E. Daskalakis, P. Bartolo, A. Weightman, G. Cooper, G. Blunn, B. Koc, Customized scaffolds for large bone defects using 3D-printed modular blocks from 2D-medical images, *Bio-Des. Manuf.* 7 (2024) 74–87, <https://doi.org/10.1007/s42242-023-00259-x>.
- [43] C.M. Murphy, M.G. Haugh, F.J. O'Brien, The effect of mean pore size on cell attachment, proliferation and migration in collagen-glycosaminoglycan scaffolds for bone tissue engineering, *Biomaterials* 31 (2010) 461–466.
- [44] F.J. O'Brien, B.A. Harley, I.V. Yannas, L.J. Gibson, The effect of pore size on cell adhesion in collagen-GAG scaffolds, *Biomaterials* 26 (2005) 433–441, <https://doi.org/10.1016/j.biomaterials.2004.02.052>.
- [45] A.H. Foroughi, D. Liu, M.J. Razavi, Simultaneous optimization of stiffness, permeability, and surface area in metallic bone scaffolds, *Int. J. Eng. Sci.* 193 (2023) 103961, <https://doi.org/10.1016/j.ijengsci.2023.103961>.
- [46] C. Lerebours, C.D.L. Thomas, J.G. Clement, P.R. Buerzli, P. Pivonka, The relationship between porosity and specific surface in human cortical bone is subject specific, *Bone* 72 (2015) 109–117, <https://doi.org/10.1016/j.bone.2014.11.016>.
- [47] C. Sandino, P. Kroliczek, D.D. McErlain, S.K. Boyd, Predicting the permeability of trabecular bone by micro-computed tomography and finite element modeling, *J. Biomech.* 47 (2014) 3129–3134, <https://doi.org/10.1016/j.jbiomech.2014.06.024>.
- [48] S.W. Chan, N. Jusoh, A. Abdul Samad, Effect of fluid properties on bone scaffold permeability, in: F. Ibrahim, J. Usman, M.Y. Ahmad, N. Hamzah (Eds.), *4th International Conference for Innovation in Biomedical Engineering and Life Sciences*, Springer Nature Switzerland, Cham, 2024, pp. 21–29, [https://doi.org/10.1007/978-3-031-56438-3\\_3](https://doi.org/10.1007/978-3-031-56438-3_3).
- [49] M.P. Nijssure, V. Kishore, Collagen-based scaffolds for bone tissue engineering applications, in: B. Li, T. Webster (Eds.), *Orthopedic Biomaterials: Advances and Applications*, Springer International Publishing, Cham, 2017, pp. 187–224, [https://doi.org/10.1007/978-3-319-73664-8\\_8](https://doi.org/10.1007/978-3-319-73664-8_8).
- [50] F.S.L. Bobbert, K. Lietaert, A.A. Eftekhar, B. Pouran, S.M. Ahmadi, H. Weinans, A. Zadpoor, Additively manufactured metallic porous biomaterials based on minimal surfaces: a unique combination of topological, mechanical, and mass transport properties, *Acta Biomater.* 53 (2017) 572–584, <https://doi.org/10.1016/j.actbio.2017.02.024>.
- [51] E.A. Nauman, K.E. Fong, T.M. Keaveny, Dependence of intertrabecular permeability on flow direction and anatomic site, *Ann. Biomed. Eng.* 27 (1999) 517–524, <https://doi.org/10.1114/1.195>.
- [52] C.-S. Shao, L.-J. Chen, R.-M. Tang, B. Zhang, J.-J. Tang, W.-N. Ma, Degradation and biological performance of porous osteomimetic biphasic calcium phosphate in vitro and in vivo, *Rare Met.* 41 (2022) 457–468, <https://doi.org/10.1007/s12598-021-01814-0>.
- [53] J. Wu, C. Feng, M. Wang, H. Wu, X. Zhu, X. Li, X. Chen, X. Zhang, Whisker of biphasic calcium phosphate ceramics: osteo-immunomodulatory behaviors, *Nano Res.* 15 (2022) 9169–9182, <https://doi.org/10.1007/s12274-022-4591-0>.
- [54] J. Wang, Y. Su, L. Xu, D. Li, Micro-patterned surface construction on BCP ceramics and the regulation on inflammation-involved osteogenic differentiation, *Mater. Sci. Eng. C* 116 (2020) 111220, <https://doi.org/10.1016/j.msec.2020.111220>.
- [55] X. Li, Y. Wang, F. Chen, X. Chen, Y. Xiao, X. Zhang, Design of macropore structure and micro-nano topography to promote the early neovascularization and osteoinductivity of biphasic calcium phosphate bioceramics, *Mater. Des.* 216 (2022) 110581, <https://doi.org/10.1016/j.matdes.2022.110581>.
- [56] Z. Tang, Y. Tan, Y. Ni, J. Wang, X. Zhu, Y. Fan, X. Chen, X. Yang, X. Zhang, Comparison of ectopic bone formation process induced by four calcium phosphate

- ceramics in mice, *Mater. Sci. Eng. C* 70 (2017) 1000–1010, <https://doi.org/10.1016/j.msec.2016.06.097>.
- [57] H. Jodati, B. Yilmaz, Z. Evis, A review of bioceramic porous scaffolds for hard tissue applications: effects of structural features, *Ceram. Int.* 46 (2020) 15725–15739, <https://doi.org/10.1016/j.ceramint.2020.03.192>.
- [58] S.J.P. Callens, R.J.C. Uyttendaele, L.E. Fratila-Apachitei, A.A. Zadpoor, Substrate curvature as a cue to guide spatiotemporal cell and tissue organization, *Biomaterials* 232 (2020) 119739, <https://doi.org/10.1016/j.biomaterials.2019.119739>.
- [59] M. Paris, A. Götz, I. Hettrich, C.M. Bidan, J.W.C. Dunlop, H. Razi, I. Zizak, D. W. Hutmacher, P. Fratzl, G.N. Duda, W. Wagermaier, A. Cipitria, Scaffold curvature-mediated novel biomimetic process originates a continuous soft tissue-to-bone interface, *Acta Biomater.* 60 (2017) 64–80, <https://doi.org/10.1016/j.actbio.2017.07.029>.
- [60] C.M. Bidan, K.P. Kommareddy, M. Rumpf, P. Kollmannsberger, Y.J.M. Bréchet, P. Fratzl, J.W.C. Dunlop, How linear tension converts to curvature: geometric control of bone tissue growth, *PLoS One* 7 (2012) e36336, <https://doi.org/10.1371/journal.pone.0036336>.
- [61] M. Werner, S.B.G. Blanquer, S.P. Haimi, G. Korus, J.W.C. Dunlop, G.N. Duda, Dirk W. Grijpma, A. Petersen, Surface curvature differentially regulates stem cell migration and differentiation via altered attachment morphology and nuclear deformation, *Adv. Sci.* 4 (2017) 1600347, <https://doi.org/10.1002/advs.201600347>.
- [62] M. Rumpler, A. Woesz, J.W.C. Dunlop, J.T. van Dongen, P. Fratzl, The effect of geometry on three-dimensional tissue growth, *J. R. Soc. Interface* (2008).
- [63] B. Liang, E. Sadeghian Dehkord, D. Van Hede, M. Barzegari, B. Verlée, J. Pirson, G. Nolens, F. Lambert, L. Geris, Model-based design to enhance neotissue formation in additively manufactured calcium-phosphate-based scaffolds, *J. Funct. Biomater.* 14 (2023) 563, <https://doi.org/10.3390/jfb14120563>.
- [64] R. Mao, Y. Lai, D. Li, Y. Huang, L. Wang, F. Luo, Y. Chen, J. Lu, X. Ge, Y. Liu, Y. Fan, X. Zhang, Q. Jiang, K. Wang, Flow channel performance in 3D printed hydroxyapatite scaffolds to improve metabolism and tissue ingrowth in flat bone repair, *Compos. B Eng.* 259 (2023) 110727, <https://doi.org/10.1016/j.compositesb.2023.110727>.
- [65] J. Rnjak-Kovacina, A.S. Weiss, Increasing the pore size of electrospun scaffolds, *Tissue Eng. Part B: Rev.* 17 (2011) 365–372, <https://doi.org/10.1089/ten.teb.2011.0235>.
- [66] A. Di Luca, A. Longoni, G. Criscenti, C. Mota, C. van Blitterswijk, L. Moroni, Toward mimicking the bone structure: design of novel hierarchical scaffolds with a tailored radial porosity gradient, *Biofabrication* 8 (2016) 045007, <https://doi.org/10.1088/1758-5090/8/4/045007>.
- [67] S.D. Dutta, J. Hexiu, M. Moniruzzaman, T.V. Patil, R. Acharya, J.S. Kim, K.-T. Lim, Tailoring osteoimmunity and hemostasis using 3D-Printed nano-photocatalytic bactericidal scaffold for augmented bone regeneration, *Biomaterials* 316 (2025) 122991, <https://doi.org/10.1016/j.biomaterials.2024.122991>.
- [68] X. Wu, K. Walsh, B.L. Hoff, G. Camci-Unal, Mineralization of biomaterials for bone tissue engineering, *Bioengineering* 7 (2020) 132, <https://doi.org/10.3390/bioengineering7040132>.
- [69] Y. Song, Z. Sun, L. Xu, Z. Shao, Preparation and characterization of highly aligned carbon nanotubes/polyacrylonitrile composite nanofibers, *Polymers* 9 (2017) 1, <https://doi.org/10.3390/polym9010001>.
- [70] A. Costa, Permeability-porosity relationship: a reexamination of the Kozeny-Carman equation based on a fractal pore-space geometry assumption, *Geophys. Res. Lett.* 33 (2006), <https://doi.org/10.1029/2005GL025134>.
- [71] A.G. Mitsak, J.M. Kemppainen, M.T. Harris, S.J. Hollister, Effect of polycaprolactone scaffold permeability on bone regeneration in vivo, *Tissue Eng.* 17 (2011) 1831–1839, <https://doi.org/10.1089/ten.tea.2010.0560>.
- [72] D. Arora, B.K. Bhunia, G. Janani, B.B. Mandal, Bioactive three-dimensional silk composite *in vitro* tumoroid model for high throughput screening of anticancer drugs, *J. Colloid Interface Sci.* 589 (2021) 438–452, <https://doi.org/10.1016/j.jcis.2021.01.010>.
- [73] S. Vermeulen, J. de Boer, Screening as a strategy to drive regenerative medicine research, *Methods* 190 (2021) 80–95, <https://doi.org/10.1016/jymeth.2020.04.004>.
- [74] W. Chen, J. Ling, K. Bai, K. Zheng, F. Yin, L. Zhang, Y. Du, High-throughput studies and machine learning for design of  $\beta$  titanium alloys with optimum properties, *Trans. Nonferrous Metals Soc. China* 34 (2024) 3194–3207, [https://doi.org/10.1016/S1003-6326\(24\)66602-1](https://doi.org/10.1016/S1003-6326(24)66602-1).
- [75] M. Zhu, H. Ye, J. Fang, C. Zhong, J. Yao, J. Park, X. Lu, F. Ren, Engineering high-resolution micropatterns directly onto titanium with optimized contact guidance to promote osteogenic differentiation and bone regeneration, *ACS Appl. Mater. Interfaces* 11 (2019) 43888–43901, <https://doi.org/10.1021/acsami.9b16050>.
- [76] S. Gobaa, S. Hoehnel, M. Roccio, A. Negro, S. Kobel, M.P. Lutolf, Artificial niche microarrays for probing single stem cell fate in high throughput, *Nat. Methods* 8 (2011) 949–955, <https://doi.org/10.1038/nmeth.1732>.
- [77] T.C. von Erlach, S. Bertazzo, M.A. Wozniak, C.-M. Horejs, S.A. Maynard, S. Attwood, B.K. Robinson, H. Autefage, C. Kallepits, A. del Río Hernández, C. S. Chen, S. Goldoni, M.M. Stevens, Cell-geometry-dependent changes in plasma membrane order direct stem cell signalling and fate, *Nat. Mater.* 17 (2018) 237–242, <https://doi.org/10.1038/s41563-017-0014-0>.
- [78] C.B. Horner, K. Hirota, J. Liu, M. Maldonado, B. Hyle Park, J. Nam, Magnitude-dependent and inversely-related osteogenic/chondrogenic differentiation of human mesenchymal stem cells under dynamic compressive strain, *J. Tissue Eng. Regenerat. Med.* 12 (2018) e637–e647, <https://doi.org/10.1002/term.2332>.
- [79] Y. Shi, H. Hu, AI accelerated discovery of self-assembling peptides, *Biomater. Translat.* 4 (2023) 291–293, <https://doi.org/10.12336/biomatertransl.2023.04.008>.
- [80] B. Kailkhura, B. Gallagher, S. Kim, A. Hiszpanski, T.Y.-J. Han, Reliable and explainable machine-learning methods for accelerated material discovery, *npj Comput. Mater.* 5 (2019) 1–9, <https://doi.org/10.1038/s41524-019-0248-2>.